Physics and Imaging in Radiation Oncology 9 (2019) 35–42

Contents lists available at ScienceDirect

Physics and Imaging in Radiation Oncology

journal homepage: www.elsevier.com/locate/phro

Original Research Article

Characterizing geometrical accuracy in clinically optimised 7T and 3T magnetic resonance images for high-precision radiation treatment of brain tumours

Jurgen Peerlings[a,b,*], Inge Compter[a], Fiere Janssen[a], Christopher J. Wiggins[c], Alida A. Postma[b], Felix M. Mottaghy[b,d], Philippe Lambin[a], Aswin L. Hoffmann[a,e,f,g]

[a] Department of Radiation Oncology (MAASTRO), GROW – School for Oncology and Developmental Biology, Maastricht University Medical Centre+, Maastricht, The Netherlands
[b] Department of Radiology and Nuclear Medicine, Maastricht University Medical Centre+, Maastricht, The Netherlands
[c] Scannexus BV, Maastricht, The Netherlands
[d] Department of Nuclear Medicine, University Hospital RWTH Aachen University, Aachen, Germany
[e] Institute of Radiooncology, Helmholtz-Zentrum Dresden-Rossendorf, Dresden, Germany
[f] OncoRay National Center for Radiation Research in Oncology, Dresden, Germany
[g] Department of Radiotherapy, University Hospital Carl Gustav Carus, Technische Universität Dresden, Dresden, Germany

ARTICLE INFO

Keywords:
Radiation treatment planning
Neuro-oncology
Ultra-high field MRI
Geometrical distortion
Diametric spherical volume
Anthropomorphic phantom

ABSTRACT

Background and purpose: In neuro-oncology, high spatial accuracy is needed for clinically acceptable high-precision radiation treatment planning (RTP). In this study, the clinical applicability of anatomically optimised 7-Tesla (7T) MR images for reliable RTP is assessed with respect to standard clinical imaging modalities.

Materials and methods: System- and phantom-related geometrical distortion (GD) were quantified on clinically-relevant MR sequences at 7T and 3T, and on CT images using a dedicated anthropomorphic head phantom incorporating a 3D grid-structure, creating 436 points-of-interest. Global GD was assessed by mean absolute deviation (MAD_{Global}). Local GD relative to the magnetic isocentre was assessed by MAD_{Local}. Using 3D displacement vectors of individual points-of-interest, GD maps were created. For clinically acceptable radiotherapy, 7T images need to meet the criteria for accurate dose delivery (GD $<$ 1 mm) and present comparable GD as tolerated in clinically standard 3T MR/CT-based RTP.

Results: MAD_{Global} in 7T and 3T images ranged from 0.3 to 2.2 mm and 0.2–0.8 mm, respectively. MAD_{Local} increased with increasing distance from the isocentre, showed an anisotropic distribution, and was significantly larger in 7T MR sequences (MAD_{Local} = 0.2–1.2 mm) than in 3T (MAD_{Local} = 0.1–0.7 mm) ($p < 0.05$). Significant differences in GD were detected between 7T images ($p < 0.001$). However, maximum MAD_{Local} remained ≤1 mm within 68.7 mm diameter spherical volume. No significant differences in GD were found between 7T and 3T protocols near the isocentre.

Conclusions: System- and phantom-related GD remained ≤1 mm in central brain regions, suggesting that 7T MR images could be implemented in radiotherapy with clinically acceptable spatial accuracy and equally tolerated GD as in 3T MR/CT-based RTP. For peripheral regions, GD should be incorporated in safety margins for treatment uncertainties. Moreover, the effects of sequence-related factors on GD needs further investigation to obtain RTP-specific MR protocols.

1. Introduction

In radiation treatment planning (RTP) of brain tumours, magnetic resonance imaging (MRI) at 1.5 or 3 Tesla (T) is currently being used as the standard anatomical imaging modality owing to its superior soft-tissue contrast compared to computer tomography (CT) [1]. Generally, after co-registration of MR and CT images, the former is used for target volume definition and the latter is used for dose calculation, as tissue electron density information is missing in MR images. However, the current clinical MR techniques are limited in depicting detailed neurologic malformations such as intracerebral tumour spread [2]. With the prospect of clinically-certified ultra-high field (UHF-)MRI systems (≥7T), images with higher signal-to-noise ratio (SNR), higher spatial resolution, and novel contrast mechanisms such as quantitative

* Corresponding author at: Maastricht University Medical Centre+, P. Debyelaan 25, P.O. Box 5800, 6202AZ Maastricht, The Netherlands.

https://doi.org/10.1016/j.phro.2018.12.001
Received 29 April 2018; Received in revised form 23 November 2018; Accepted 5 December 2018

susceptibility-weighted images will become available, enabling the visualisation of small lesions, basal ganglia, and tumour angiogenesis [3–5]. The improved ability in detecting microvasculature (diameter ~100 μm) could play a decisive role in staging primary brain tumours such as glioblastoma (GBM), as tumour angiogenesis is directly associated with tumour grade, and could aid in determining relevant location of dedifferentiated cells for image-guided biopsies [6,7]. In addition, 7T MRI could aid target volume definition in RTP by visualising microvasculature outside the contrast-enhanced tumour and infiltration of GBM cells along white matter tracts [7–9]. During follow-up scans, 7T MRI has been shown to reveal radiation-induced microbleeds, indicating potential neurocognitive decline and the need to adapt RTP [10,11].

However, concerns regarding geometrical distortion (GD) with increasing static magnetic field strength (B_0) have compromised the integration of UHF-MRI into radiation treatment planning. System-related GD are mainly induced by imperfections in hardware (B_0-inhomogeneity, gradient field nonlinearity, and eddy currents), applied gradient pulse scheme and parameter settings (sequence-dependent GD), while phantom-related GD (chemical shift and susceptibility differences) are related to the object's shape placed in the MR system [12,13]. To be applicable for high-precision RTP, the spatial accuracy of anatomical images needs to be within 2 mm for non-stereotactic radiotherapy and within 1 mm for stereotactic radiotherapy, as is the case for 3T MRI [13–18]. In fact, profound GD may have significant dosimetric impact in radiotherapy as the precision of beam targeting and dose calculations could be affected [19,20]. For high-precision dose delivery techniques that apply steep 3D dose gradients (intracranial stereotactic radiotherapy or radiosurgery), spatial inaccuracies of > 1 mm could result in clinically unacceptable dose variations of more than 15% that could lead to underdosage of target volume and/or overdosage of surrounding tissue [20,21]. Ultimately, inaccuracy of beam targeting and dose calculation could lead to a different clinical outcome and local tumour control [13,18]. For instance, techniques that apply extremely steep dose gradients, such as stereotactic radiotherapy and radiosurgery, are susceptible to significant dosimetric effects (5–32% underdosage) caused by even small GD of 1.3 mm [21,22]. The question therefore arises whether our clinical 7T MRI protocol, optimised for anatomical imaging, can produce images with acceptable spatial accuracy needed for reliable high-precision radiation treatment of brain tumours. Previously several investigators have evaluated geometrical distortion on either CT, 3T or 7T MRI, demonstrating a maximum GD of up to several mm in large cylindrical or cubical phantoms [14,23–27].

This study aims to investigate the clinical applicability of anatomical 7T MRI in comparison to 3T MRI and CT for reliable high-precision radiotherapy by evaluating the magnitude and location of hardware-related GD. We hypothesise: 1) acceptable submillimetre spatial accuracy could be achieved in our 7T MRI protocol and no significant differences in GD are present between different 7T sequences; 2) the tolerated level of GD in 7T MRI is not significantly different from system-related GD in a predefined 3T MRI protocol, clinically used for RTP. To test these hypotheses on both global level (GD throughout the entire volume-of-interest (VOI)) and on local level (GD relative to the distance from the magnetic isocentre), we performed quantitative image analyses using a dedicated anthropomorphic head phantom in a clinically realistic set-up. Hence, different sequence parameter settings and distortion correction methods were not explored in this study.

2. Materials and methods

2.1. Phantom

A dedicated anthropomorphic head phantom (CIRS Model 603A, Computerized Imaging Reference Systems Inc., USA) was used to evaluate system-related GD in 7T MRI, 3T MRI, and CT images (Fig. S.1). The anatomical shape demanded similar procedures used for clinically imaging patients (FOV setting, shimming, robust positioning inside the scanner and head coil). Furthermore, the centre of the phantom was aligned with the magnetic isocentre.

The phantom was composed of a plastic-based bone substitute and soft-tissue equivalent fluid consisting of a water-based polyacrylamide with added $NiCl_2$ (Zerdine®, CIRS). Inside the phantom, 3-mm thick nylon rods formed a 3D grid with 15 mm spacing (± 0.05 mm manufacturing tolerance), defining a VOI of 15 × 12 × 13.5 cm^3 (anterior-posterior (AP) × left–right (LR) × superior-inferior (SI)). At grid-intersections, 437 measurable points-of-interest (POIs) were identified. Nylon shows similar magnetic susceptibility properties to water (χ < 3 ppm) and was assumed not to induce such susceptibility artefacts in spin-echo or gradient-echo sequences [24,28].

2.2. Image acquisition

MR images were acquired on a 7T MR system (Magnetom 7T, Siemens, DEU) and on a 3T MR system (Achieva 3T, Philips, NL) using 32-channel head coils from Nova Medical inc. (1Tx/32Rx, Wilmington, USA) and Invivo Corp. (Florida, USA), respectively. The 7T MR system was equipped with Siemens' SC72-gradient system (80 mT/m peak gradient amplitude, 200 T/m/s maximum slew rate). The 3T MR system was fitted with Philips' Dual Quasar gradient system (80 mT/m peak gradient amplitude, 100 mT/m/s maximum slew rate). Magnetic field homogeneity specification were described as < 5 ppm pk-pk and ≤1.1 ppm at a diameter of a spherical volume (DSV) of 45 cm, respectively. All MR sequences were previously optimised to acquire anatomical images of high image quality within an acceptable scan duration, and were not altered for this study [9]. The selected 7T MR sequences included magnetization-prepared rapid gradient-echo (MP2RAGE), T2-sampling perfection with application optimized contrasts using different flip angle evolution (T2-SPACE), T2-SPACE with fluid attenuation inversion recovery (T2-SPACE FLAIR), and multi-echo gradient-echo (T1-GRE) [9]. Sequences with equivalent pulse schemes were selected from a predefined clinical 3T MR protocol used in RTP and included turbo field echo (3D TFE), volume isotropic turbo spin-echo (T2-VISTA) with and without FLAIR, and fast field gradient echo (T1-FFE), respectively (Table S.1). Vendor-installed 3D distortion correction methods were applied to restore gradient non-linearity and 3D volume-based second order shimming procedures were applied to improve B_0-homogeneity [14,29,30].

CT images were acquired (SOMATOM Sensation 10, Siemens, Germany) with a slice thickness of 1 mm, 306 slices, 50 × 50 cm^2 FOV, 140 kV, and 400 mAs.

2.3. Methods of analyses

The known 3D coordinates of all POIs were defined as reference dataset and manually reconstructed in MRI and CT images using Eclipse treatment planning system (Varian Medical Systems, USA). The X-, Y-, and Z-axes defined the LR-, SI-, and AP-directions in both datasets, respectively.

Three methods were used to assess GD at different levels of sophistication using in-house developed MATLAB software (R2014b, MathWorks Inc, USA) (Fig. 1). Firstly, mean absolute deviation (MAD) was computed to assess GD on a global level (MAD_{Global}) throughout the entire VOI, independently of location within the phantom. Secondly, MAD was calculated to assess GD on a local level (MAD_{Local}) relative to the distance from the magnetic isocentre. MAD was calculated according to:

$$MAD(i) = \frac{1}{N(i)} \sum_{j=1}^{N(i)} | D_i(j) - \delta_i | \quad (1)$$

where $i = 1 \ldots M$ is an index into set $\Delta = \{\delta_1, \delta_2, \cdots, \delta_M\}$ of M unique

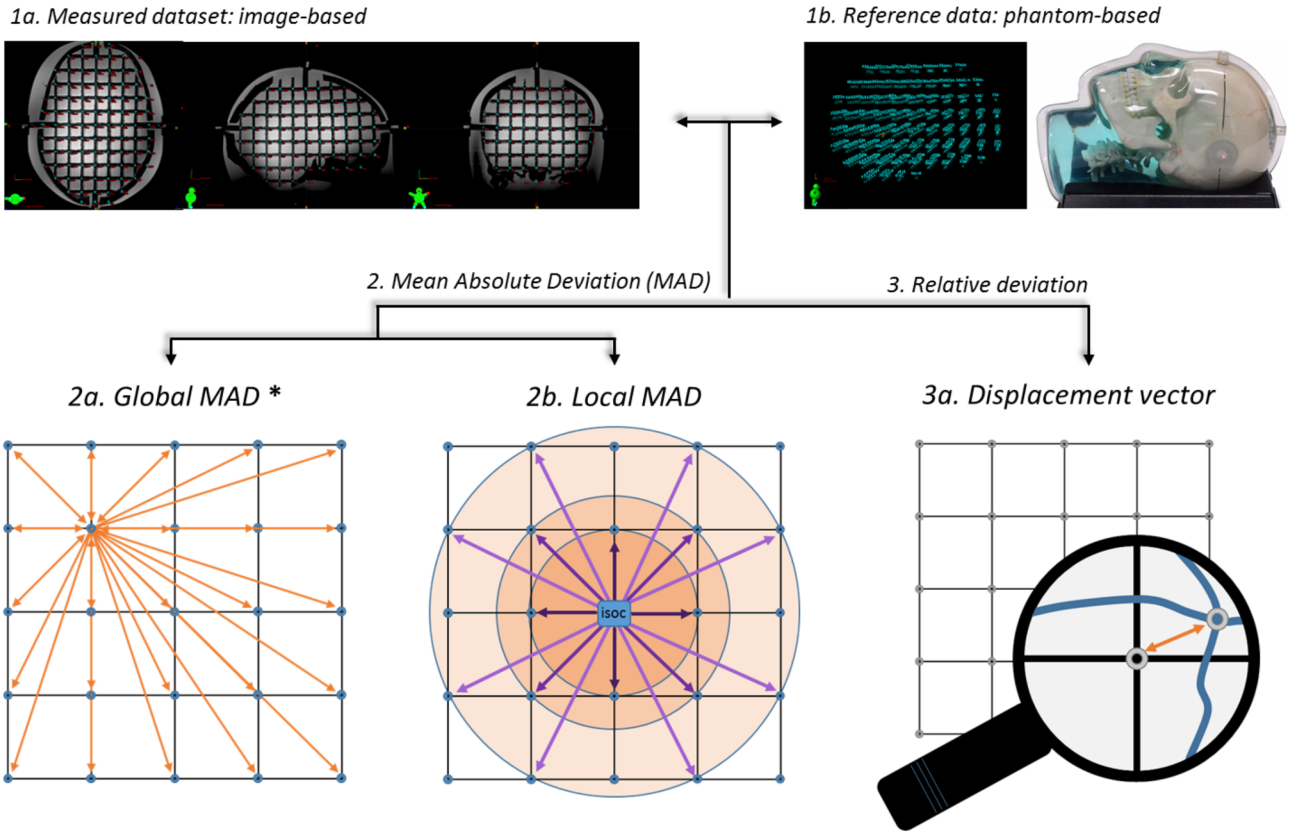

Fig. 1. Overview of 3D data acquisition and analyses. XYZ-coordinates are determined on CT and MR images (1a.), and based on product characteristics of the CIRS' phantom model 603A (1b.). Global MAD (2a.) is based on distances with 2 variable grid-intersection points (*example given for 1 intersection but applies for all points). Local MAD (2b.) is based on distances between magnetic field isocentre and 1 variable grid-intersection points. Displacements vectors (3a.) are determined between the measured and reference coordinates of each individual data-point and indicate the relative 3D geometrical distortion.

distances, $D_i(j)$ is the measured Euclidean distance for the j-th unique pair of POIs having an Euclidean distance δ_i in the reference dataset, and $N(i)$ represents the number of unique pairs of POIs. For MAD_{Global}, Δ contained all unique distances that could be observed within the entire phantom. For MAD_{Local}, Δ contained only unique distances that originate from the POI nearest the magnetic isocentre. The mean MAD was averaged over all M unique distances in Δ.

The third method of analyses pin-pointed GD by calculating 3D displacement of each individual POI by computing the Euclidean distance directly between the POI-coordinates in the image (X_m, Y_m, Z_m) and the coordinates in the reference datasets (X_{ref}, Y_{ref}, Z_{ref}):

$$D_{xyz} = \sqrt{(X_m - X_{ref})^2 + (Y_m - Y_{ref})^2 + (Z_m + Z_{ref})^2} \quad (2)$$

The resulting 3D displacement vector (D_{xyz}) indicated relative GD of each individual POI, independently of all other POIs.

The three methods of analyses provided complementary information on the geometrical quality of the images. The MAD_{Global} quantified the level of GD throughout the entire VOI, thereby ignoring information on the absolute and relative locations of the POIs. The MAD_{Local} retained spatial information by quantifying the GD with respect to the DSV at the magnetic isocentre. To quantify spatial integrity of an entire image, 95% confidence interval ($|CI_{95}|$) was calculated from MAD and standard deviation (SD) as:

$$|CI_{95}| = MAD + 2SD \quad (3)$$

Based on this interval, a maximum acceptability-level of 1 mm was defined. The level of GD was considered acceptable when $MAD_{Local} \leq 1$ mm (at a specific DSV) and $|CI_{95}| \leq 1$ mm.

2.4. Statistical analyses

To assess differences in sequence-dependent GD, MAD_{Global} and MAD_{Local} were analysed between 7T MRI sequences and between 3T MRI sequences using a Kruskal-Wallis test. To assess differences in tolerated GD-levels, MAD_{Global} and MAD_{Local} were analysed between equivalent sequence pulse schemes in 7T and 3T MRI using a multiple student t-test with Bonferonni-Sidak correction. For MAD_{Local}, DSV at which statistical significance in MAD_{Local} between sequences occurred, was identified by a separate Kruskal-Wallis test for each set of unique distances. All statistical analyses were performed using GraphPad Prism v6.01 (GraphPad, USA). P-values < 0.05 were considered to indicate statistical significance.

3. Results

3.1. Global GD

In total, 95.266 pairs of distances were identified and binned into 100 unique distances, ranging from 15 mm to 164.3 mm. In CT images, MAD_{Global} ranged from 0.1–0.6 mm with mean MAD_{Global} of 0.3 ± 0.1 mm. For MR images, MAD_{Global} ranged from 0.3–2.2 mm and 0.2–0.8 mm in 7T and 3T MRI, respectively (Table 1, Fig. 2). Based on $|CI_{95}|$, only 3T MR sequences presented GD < 1 mm throughout the entire image. No statistical significance in MAD_{Global} were found between 7T MR images ($P = 0.38$) or 3T MR images ($P = 0.13$). However, significant differences in MAD_{Global} were detected between all equivalent sequences on 7T and 3T MR system ($P < 0.001$) (Fig. 3.).

Table 1
Global geometrical deformation as measured on 3T and 7T MRI (*** = P < 0.001).

		MAD_{Global} (in mm)					MAD_{Global} (in mm)			
B_0	Sequence	Range	Mean ± sd	$\|CI_{95}\|$	B_0	Sequence	Range	Mean ± sd	$\|CI_{95}\|$	*P* value
7T	MP2RAGE	0.3–1.9	1.0 ± 0.3	1.7	3T	3D TFE	0.22–0.51	0.27 ± 0.23	0.7	***
	SPACE	0.3–2.0	1.0 ± 0.4	1.7		T2-VISTA	0.20–0.70	0.26 ± 0.20	0.7	***
	SPACEFLAIR	0.3–2.2	0.9 ± 0.3	1.6		T2-VISTA FLAIR	0.19–0.62	0.29 ± 0.23	0.7	***
	GRE	0.3–1.9	1.0 ± 0.4	1.8		T1-FFE	0.3–0.7	0.4 ± 0.3	1.0	***

3.2. Local GD

In CT images, MAD_{Local} ranged from 0.1 to 0.3 mm with mean MAD_{Local} of 0.2 ± 0.04 mm (Fig. 4). All MR images acquired at 7T presented a steady increase in MAD_{Local} with increasing distance from the magnetic isocentre. MAD_{Local} ranged from 0.2–1.8 mm for 7T MRI and from 0.1–0.7 mm for 3T MRI. Each 7T MR sequence remained below the clinical tolerance-level of 1 mm up until a defined DSV (Table 2). For T1-GRE, MAD_{Local} exceeded 1 mm only at DSV of 87.5–88.7 mm.

For all 3T MR sequences, MAD_{Local} remained below 1 mm throughout the whole VOI. MAD_{Local} of MP2RAGE was statistically greater than all other 7T MR sequences (P < 0.001, Fig. S.2). No significant difference in MAD_{Local} was found between T2-SPACE, T2-SPACE FLAIR (P = 0.064), and T1-GRE (P = 0.093), respectively. Within the 3T dataset, MAD_{Local} of 3D TFE was significantly different from T2-VISTA (P < 0.001), T2-VISTA FLAIR (P = 0.046), and T1-FFE (P < 0.001). T2-VISTA FLAIR presented significantly different MAD_{Local} from T1-FFE (P < 0.001). MAD_{Local} was not significantly different between T1-FFE and T2-VISTA (P = 0.51), and the T2-VISTA and T2-VISTA FLAIR sequences (P = 0.061). However, all sequences met the criteria for GD and seemed to have found an equilibrium with requirements for anatomical imaging.

Statistical analyses of MAD_{Local} between equivalent 7T and 3T sequences indicated significant differences for all sequences (P < 0.001). However, no significant difference in MAD_{Local} was found between equivalent sequences when the DSV was considered (Table 2).

3.3. 3D displacement

The magnitude of each displacement vector is presented in a 2D mesh-plot in axial (XZ), coronal (XY), and sagittal (YZ) planes, intersecting the magnetic isocentre. The worst GD was presented in MP2RAGE and 3D TFE (Fig. 4). Additionally, anisotropic distributions of GD were observed along the phase-encoding direction and frequency-encoding direction. Particularly the anterior–superior section was affected by spatial deformation and maximal GD was observed in the right-superior section of the anterior region (frontal lobe). Distortion maps of all sequences are presented in Figs. S.3–5.

4. Discussion

This study reports both system- and phantom-related GD on clinically-relevant MR sequences at 7T MRI for neurological imaging and allows direct comparison to GD on both 3T MRI and CT images. System-related GD was present in all 3T and 7T MRI and increased with increasing distance from the magnetic isocentre, even though vendor-provided correction methods and 2nd order 3D shimming were applied. However, GD of ≤1 mm could be assured within a sequence-dependent DSV near the magnetic isocentre.

While UHF-MRI promises clinical gain in terms of spatial resolution, SNR, contrast, and delineation of pathology, implementation of 7T MRI in RTP requires mm-scale spatial accuracy for reliable, high-precision radiotherapy. This geometrical requirement was met by all 3T MR sequences throughout the entire VOI while the magnitude of GD in 7T MRI depended on the distance from the magnetic isocentre and applied sequence. GD ≤ 1 mm was apparent in 7T MRI within a sequence-specific DSV. Moreover, no significant differences in system-related GD were found between 3T and 7T images near the magnetic isocentre. This implies that these 7T MRI with clinically acceptable/tolerable levels of spatial uncertainty could be applied for high-precision RTP in central brain regions, under the assumption that tissue-related GD is negligible. In addition, it has previously been shown that GD in 7T MRI did not affect targeting of basal ganglia and subthalamic nuclei in deep-brain stimulation [23,31].

Some sequences are more prone to GD than others as gradient pulse scheme and parameter settings affect B_0-homogeneity and eddy currents [25,29,32]. Our MP2RAGE sequence, which acquires 2 gradient-echo images at different inversion times, presented the largest GD at 7T (and smallest DSV where GD < 1 mm) [33]. Nevertheless, even in this worst-case scenario, system-related GD at 7T was below the clinically acceptable limit of ≤1 mm within 68.7 mm DSV. Presumably, GD in MP2RAGE could be related to the combination of different sequence parameter settings (receiver bandwidth (rBW), FOV, and matrix size) [13,14,25,29,31,32,34]. The effect of varying rBW on GD and SNR has extensively been studied by Walker et al. (2014) in 4 different MR systems [31]. For instance, increasing rBW would reduce GD, chemical shift, and susceptibility artefacts but would also reduce SNR. Limiting FOV settings (i.e., fewer acquisition lines in k-space) could subside the impact of time-dependent off-resonance effects, reducing GD [34,35]. However, this could also influence spatial resolution, SNR, and induce potential fold-over artefacts.

Residual GD in phase-encoding direction is expected to be related to gradient non-uniform and could be adequately reduced by vendor-installed distortion correction methods [14,18,25,26]. The technique behind this correction is similar for all main MR manufacturers and achieve comparable and reproducible results for 3T and 7T MRI [4,14,15,18,31]. Nonetheless, some residual system-dependent GD was detected in this study despite applying correction methods and 3D shimming. It is therefore important to note that vendor-provided distortion correction is not flawless, uncorrected B_0-inhomogeneity and eddy currents could still induce GD, and gradient coils are designed with a tolerated performance variation [24,36]. For example, general gradient errors of body gradient coils should be > 2% of the gradient strength over a 40 cm DSV[37,38].

Our findings of GD corresponded well with literature. At 3T, Stanescu et al. reported maximal overall GD of 0.6 mm in 3D TFE sequences and Schmidt et al. have shown global GD of less than 0.5 mm in an IR-sequence (rBW = 890 Hz/pixel, resolution 1 mm^3) [14,39]. However, some studies report GD of several centimetres [25–27]. These findings, however, occurred at the edge of the scanner's FOV on a large cubical phantom that was placed in a body coil. In contrast to this, we used a dedicated anthropomorphic head phantom to mimic a clinically realistic scan procedure with standard radiofrequency coils, shimming, distortion correction, and FOV settings (≤256 mm).

Similar to our approach and FOV setting, Dammann et al. investigated hardware-related GD in 7T MRI using a cylindrical phantom (190 POIs) and presented local GD smaller than 1 mm at < 80 mm DSV, except in T2-TSE (rBW = 350 Hz/pixel, resolution 0.6 mm^2) that showed maximal local GD of 1.6 mm [26]. Presumably, this sequence

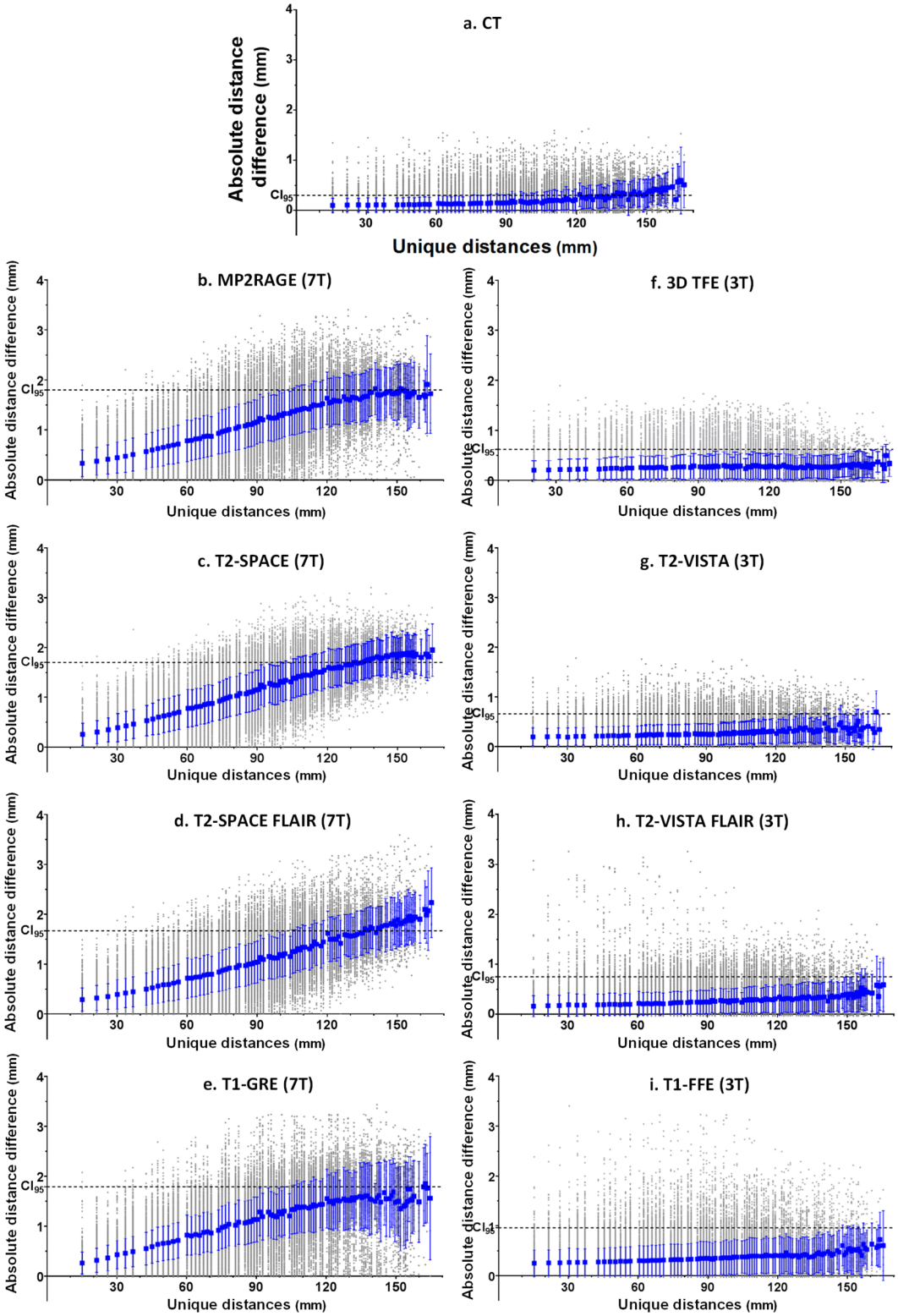

Fig. 2. Absolute differences in Euclidian distance between the measured and reference dataset (*grey dot*) relative to the unique distances found in the reference dataset, observed within CT (a), MP2RAGE (b), T2-SPACE (c), T2-SPACE FLAIR (d), T1-GRE (e), 3D TFE (f), T2-VISTA (g), T2-VISTA FLAIR (h), T1-FFE (i). The overall geometric distortion was quantified by MAD_{Global} (± SD) (*blue square*). The 95% confidence interval (CI_{95}) is shown as the dotted horizontal line. (For interpretation of the references to colour in this figure legend, the reader is referred to the web version of this article.)

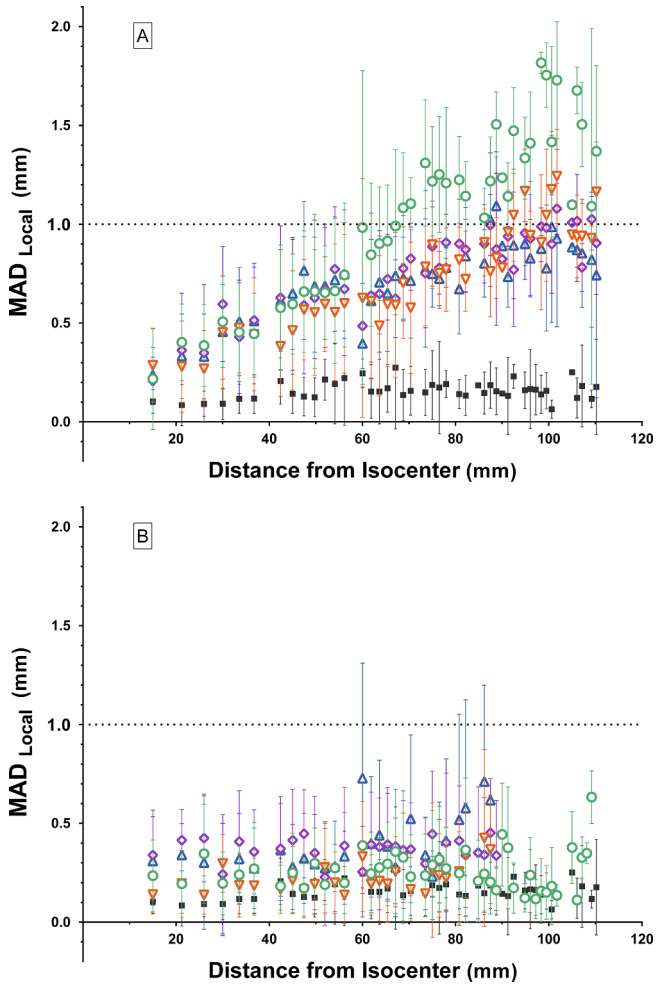

Fig. 3. MAD_{Local} values (± SD) relative to the distance from the magnetic isocentre at 7T (a) and 3T (b) MRI, both relative to CT (*black square*). Presented 7T MR sequence include MP2RAGE (*green circle*), T2-SPACE (*purple diamond*), T2-SPACE FLAIR (*orange downward triangle*), and T1-GRE (*blue upward triangle*). The same colour- and shape-code was used for the equivalent 3T sequences, 3D TFE, T2-VISTA, T2-VISTA FLAIR, and T1-FFE, respectively. The dotted horizontal line represents the 1 mm-acceptability level required for spatially reliable RTP. (For interpretation of the references to colour in this figure legend, the reader is referred to the web version of this article.)

was affected by intravoxel dephasing, image blurring and inaccurate measurements at the phantom's edge [26]. This could also could explain our finding of 1.2 mm local GD at 80 mm DSV. Differences in rBW-setting could explain GD differences found in MPRAGE (rBW = 600 Hz/pixel, resolution 1 mm^3) and MP2RAGE (rBW = 248 Hz/pixel, 0.7 mm^3). Recently, Lau et al. demonstrated differences in local GD between 3T and 7T larger than 1 mm at 80 mm DSV for T1-MPRAGE (rBW = 195 Hz/px, 1 mm^3) [4]. In our study, MP2RAGE showed differences in MAD_{Local} between 3T and 7T to be below 1 mm up for a ≤87.5 mm DSV.

Distortion maps of MP2RAGE indicated an anisotropic distribution of GD along the phase-encoding (AP) and frequency-encoding (SI) direction (Fig. 4). In a comparable 7T phantom study by Cho et al., coronal distortion maps showed 0.4 mm GD along the frequency-encoding direction and 0.8 mm along the phase-encoding direction [22].

We observed GD in CT images with MAD_{Global} ranging from 0.1 to 0.6 mm and MAD_{Local} ranging from 0.1 to 0.3 mm. These findings were unanticipated as it is generally recognized that CT images are distortion-free. Other studies have merged MRI with CT, ignoring this innate GD and measured fundamental errors. Artefacts in CT images could originate from incorrectly reported scanner table speed or shearing distortion (incorrectly reported gantry tilt or table bending). In this study, GD in CT images could represent partial volume effects and variations in manual reconstruction leading to slightly different xyz-coordinates measurements of POIs (experimental inaccuracies).

In this study, we limited ourselves to evaluating system-related GD and not tissue-related GD. Relative to system-related GD, tissue-induced GD is rather small in 3T sequences that are currently being used for RTP of brain tumours, but it is nevertheless not negligible [16]. Simulations on 3T MRI suggest that susceptibility-induced GD were on average 0.6 mm at cranial air cavities [40]. This has recently been confirmed by Schmidt et al., who specified susceptibility-related GD of 0.4 mm in the naso-oropharyngeal cavities and around the internal ear canal using a T1-weighted sequence (rBW = 890 Hz/pixel, resolution 1 mm^3) [14]. It remains to be determined what the impact of tissue-related GD is for 7T MRI. Susceptibility artefacts are proportional to the magnetic field strength and TE but could be reduced by increasing rBW [12]. Regardless, patient-specific correction methods are required [16,37,40]. Recently, Rai et al. (2018) developed an 3D printed human skull with sinuses and mastoid air cells, water-based brain tissue and eyes and surrogate cortical bone [41]. Such realistic anatomical skulls could be used to further assess tissue-induced GD in simulated air cavities, bony anatomy, and soft tissue. Since system-related GD could be further reduced by appropriate setting of MR sequence parameters, research has been performed to systematically assess the impact of e.g., rBW, FOV, matrix size, scanning direction, and various (post-)processing correction algorithms [16,18,27,31,36]. However, 7T MR protocols need to be optimised specifically for each clinical application and the trade-off between anatomical image quality (spatial resolution, SNR, visibility of pathology) and image integrity (spatial accuracy) needs to be made, while respecting specific absorption rate restriction [29,32]. For example, high-precision RTP relies heavily on high geometrical accuracy but could compensate on image resolution, while in radiology larger GD could be tolerated.

To apply 7T images in radiotherapy, GD should be ≤1 mm to ensure reliable RTP and dose delivery with local dose variations less than 5–10% [21]. This strict criterion was met by all the clinically relevant sequences we tested on 3T and 7T MRI up until 92.5–101.7 mm DSV around the magnetic isocentre, except for the MP2RAGE sequence. Delineations of brain lesions and organs-at-risk in the frontal or occipital lobe on 7T MRI can be significantly influenced by GD as the spatial uncertainty exceeds 1 mm in these regions. Even though systematic and random treatment uncertainties are foreseen in a planning treatment volume (PTV), the degree and location of GD is rarely taken into account during radiation dose planning. This study has shown that system-related GD should be incorporated into the PTV margin to achieve a high level of dose delivery accuracy for intracranial (stereotactic) radiotherapy. This can be accomplished by incorporating the GD present at the tumour location within a margin recipe for dose delivery as suggested by Van Herk et al. and Seravelli et al. [42,43]. We therefore recommend applying larger tumour site-specific PTV margins in regions where spatial integrity of 7T MRI could not be warranted within 1 mm. Apart from adjustment of PTV margins, it is advised to find a trade-off between image quality and image distortion, and apply MR imaging protocols that are dedicated for RTP purposes.

In conclusion, GD of ≤1 mm could be assured within a sequence-dependent DSV near the magnetic isocentre, implying that this 7T MRI protocol could be applied with clinically acceptable/tolerable levels of spatial uncertainty for high-precision RTP in central brain regions, under the assumption that tissue-related GD can be ignored. For peripheral regions, 7T MR protocol for RTP should incorporate GD in tumour-site specific PTV margins for treatment uncertainties. Nevertheless, dedicated MR protocols are aspired for application in radiation oncology and further optimisation of sequence parameter settings and GD reduction methods are needed.

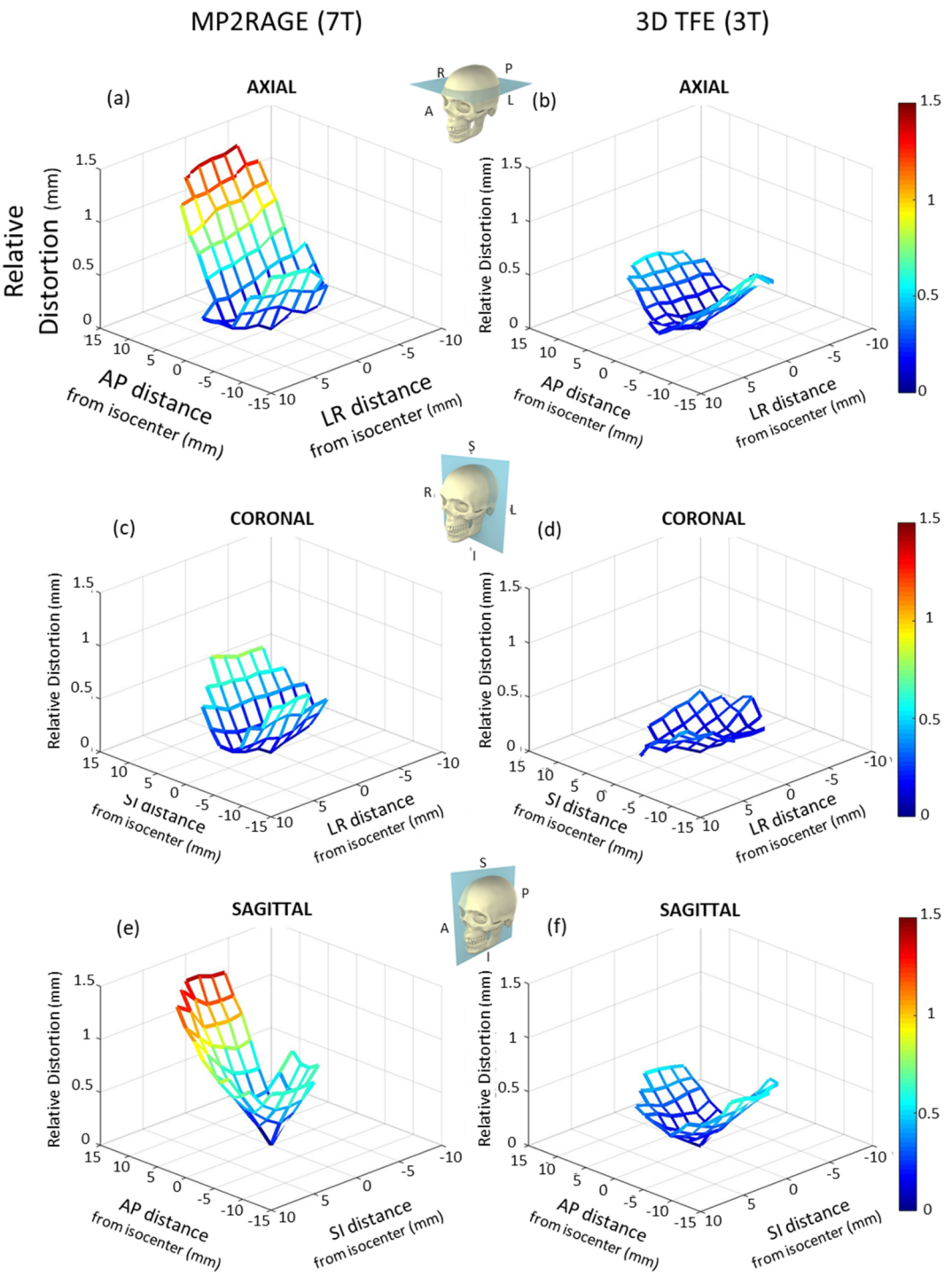

Fig. 4. Distortion maps of MP2RAGE on 7T MRI (a) and 3D TFE on 3T MRI (b) measured in the axial plane nearest the magnetic isocentre (Y = 0), in the coronal plane (Z = 0), and in the sagittal plane (X = 0).

Table 2
Local geometrical deformation as measured on 3T and 7T MRI (*** = P < 0.001, § = DSV at which statistical significance between sequences occurred).

		MAD_{Local} (in mm)						MAD_{Local} (in mm)					*P* value
B_0	Sequence	Range	Mean ± sd	$\|CI_{95}\|$	< 1 mm at DSV	B_0	Sequence	Range	Mean ± sd	$\|CI_{95}\|$	< 1 mm at DSV	Sign.	*P* < 0.05 at DSV§
7T	MP2RAGE	0.2–1.8	0.8 ± 0.3	1.4	69	3T	3D TFE	0.1–0.6	0.3 ± 0.2	0.6	all	***	42
	SPACE	0.2–1.18	0.7 ± 0.3	1.2	102		T2-VISTA	0.2–0.4	0.4 ± 0.3	0.9	all	***	69
	SPACEFLAIR	0.3–1.2	0.6 ± 0.3	1.2	93		T2- VISTA FLAIR	0.1–0.4	0.2 ± 0.2	0.5	all	***	47
	GRE	0.2–1.1	0.7 ± 0.3	1.3	87–89		T1-FFE	0.2–0.7	0.3 ± 0.3	0.9	all	***	45–56

Disclosure of interest

The authors report no conflict of interest.

Appendix A. Supplementary data

Supplementary data to this article can be found online at https://doi.org/10.1016/j.phro.2018.12.001.

References

[1] Niyazi M, Brada M, Chalmers AJ, Combs SE, Erridge SC, Fiorentino A, et al. ESTRO-ACROP guideline "target delineation of glioblastomas". Radiother Oncol 2016;118:35–42. https://doi.org/10.1016/j.radonc.2015.12.003.

[2] Claes A, Idema AJ, Wesseling P. Diffuse glioma growth: a guerilla war. Acta Neuropathol 2007;114:443–58. https://doi.org/10.1007/s00401-007-0293-7.

[3] Barrett TF, Sarkiss CA, Dyvorne HA, Lee J, Balchandani P, Shrivastava RK. Application of ultrahigh field magnetic resonance imaging in the treatment of brain tumors: a meta-analysis. World Neurosurg 2016;86:450–65. https://doi.org/10.1016/j.wneu.2015.09.048.

[4] Lau JC, Khan AR, Zeng TY, MacDougall KW, Parrent AG, Peters TM. Quantification of local geometric distortion in structural magnetic resonance images: application to ultra-high fields. Neuroimage 2017. https://doi.org/10.1016/j.neuroimage.2016.12.066.

[5] Trattnig S, Bogner W, Gruber S, Szomolanyi P, Juras V, Robinson S, et al. Clinical applications at ultrahigh field (7 T). Where does it make the difference? NMR Biomed 2016;29:1316–34. https://doi.org/10.1002/nbm.3272.

[6] Trattnig S, Springer E, Bogner W, Hangel G, Strasser B, Dymerska B, et al. Key clinical benefits of neuroimaging at 7T. Neuroimage 2016. https://doi.org/10.1016/j.neuroimage.2016.11.031.

[7] Christoforidis GA, Yang M, Abduljalil A, Chaudhury AR, Newton HB, McGregor JM, et al. "Tumoral pseudoblush" identified within gliomas at high-spatial-resolution ultrahigh-field-strength gradient-echo MR imaging corresponds to microvascularity at stereotactic biopsy. Radiology 2012;264:210–7. radiol.12110799 [pii]10.1148/radiol.

[8] Moenninghoff C, Maderwald S, Theysohn JM, Kraff O, Ladd ME, El Hindy N, et al. Imaging of adult astrocytic brain tumours with 7 T MRI: preliminary results. Eur Radiol 2010;20:704–13. https://doi.org/10.1007/s00330-009-1592-2.

[9] Compter I, Peerlings J, Eekers DB, Postma AA, Ivanov D, Wiggins CJ, et al. Technical feasibility of integrating 7 T anatomical MRI in image-guided radiotherapy of glioblastoma: a preparatory study. MAGMA 2016;29:591–603. https://doi.org/10.1007/s10334-016-0534-7.

[10] Bian W, Hess CP, Chang SM, Nelson SJ, Lupo JM. Susceptibility-weighted MR imaging of radiation therapy-induced cerebral microbleeds in patients with glioma: a comparison between 3T and 7T. Neuroradiology 2014;56:91–6. https://doi.org/10.1007/s00234-013-1297-8.

[11] Lupo JM, Chuang CF, Chang SM, Barani IJ, Jimenez B, Hess CP, et al. 7-Tesla susceptibility-weighted imaging to assess the effects of radiotherapy on normal-appearing brain in patients with glioma. Int J Radiat Oncol Biol Phys. 2012;82.e493 e500 S0360-3016(11)02787-8 [pii] 10.1016/j.ijrobp.2011.05.046.

[12] Dietrich O, Reiser MF, Schoenberg SO. Artifacts in 3-T MRI: physical background and reduction strategies. Eur J Radiol 2008;65:29–35. https://doi.org/10.1016/j.ejrad.2007.11.005.

[13] Weygand J, Fuller CD, Ibbott GS, Mohamed AS, Ding Y, Yang J, et al. Spatial precision in magnetic resonance imaging-guided radiation therapy: the role of geometric distortion. Int J Radiat Oncol Biol Phys 2016;95:1304–16. https://doi.org/10.1016/j.ijrobp.2016.02.059.

[14] Schmidt MA, Wells EJ, Davison K, Riddell AM, Welsh L, Saran F. Stereotactic radiosurgery planning of vestibular schwannomas: Is MRI at 3 tesla geometrically accurate? Med Phys 2016. https://doi.org/10.1002/mp.12068.

[15] Torfeh T, Hammoud R, Perkins G, McGarry M, Aouadi S, Celik A, et al. Characterization of 3D geometric distortion of magnetic resonance imaging scanners commissioned for radiation therapy planning. Magn Reson Imaging 2016;34:645–53. https://doi.org/10.1016/j.mri.2016.01.001.

[16] Wang H, Balter J, Cao Y. Patient-induced susceptibility effect on geometric distortion of clinical brain MRI for radiation treatment planning on a 3T scanner. Phys Med Biol 2013;58:465–77. https://doi.org/10.1088/0031-9155/58/3/465.

[17] Klein EE, Hanley J, Bayouth J, Yin FF, Simon W, Dresser S, et al. Task Group 142 report: quality assurance of medical accelerators. Med Phys 2009;36:4197–212. https://doi.org/10.1118/1.3190392.

[18] Duchin Y, Abosch A, Yacoub E, Sapiro G, Harel N. Feasibility of using ultra-high field (7 T) MRI for clinical surgical targeting. PLoS One 2012;7:e37328https://doi.org/10.1371/journal.pone.0037328.

[19] Jursinic PA, Rickert K, Gennarelli TA, Schultz CJ. Effect of image uncertainty on the dosimetry of trigeminal neuralgia irradiation. Int J Radiat Oncol Biol Phys 2005;62:1559–67. https://doi.org/10.1016/j.ijrobp.2005.01.059.

[20] Karaiskos P, Moutsatsos A, Pappas E, Georgiou E, Roussakis A, Torrens M, et al. A simple and efficient methodology to improve geometric accuracy in gamma knife radiation surgery: implementation in multiple brain metastases. Int J Radiat Oncol Biol Phys 2014;90:1234–41. https://doi.org/10.1016/j.ijrobp.2014.08.349.

[21] Seibert TM, White NS, Kim GY, Moiseenko V, McDonald CR, Farid N, et al. Distortion inherent to magnetic resonance imaging can lead to geometric miss in radiosurgery planning. Pract Radiat Oncol. 2016;6:e319–28. https://doi.org/10.1016/j.prro.2016.05.008.

[22] Cho ZH, Min HK, Oh SH, Han JY, Park CW, Chi JG, et al. Direct visualization of deep brain stimulation targets in Parkinson disease with the use of 7-tesla magnetic resonance imaging. J Neurosurg 2010;113:639–47. https://doi.org/10.3171/2010.3.jns091385.

[23] Wang D, Doddrell DM. Geometric distortion in structural magnetic resonance imaging. Curr Med Imaging Rev 2005;1:49–60.

[24] O'Callaghan J, Wells J, Richardson S, Holmes H, Yu Y, Walker-Samuel S, et al. Is your system calibrated? MRI gradient system calibration for pre-clinical, high-resolution imaging. PLoS One 2014;9:e96568https://doi.org/10.1371/journal.pone.0096568.

[25] Baldwin LN, Wachowicz K, Thomas SD, Rivest R, Fallone BG. Characterization, prediction, and correction of geometric distortion in 3 T MR images. Med Phys 2007;34:388–99.

[26] Dammann P, Kraff O, Wrede KH, Ozkan N, Orzada S, Mueller OM, et al. Evaluation of hardware-related geometrical distortion in structural MRI at 7 Tesla for image-guided applications in neurosurgery. Acad Radiol 2011;18:910–6. https://doi.org/10.1016/j.acra.2011.02.011.

[27] Doran SJ, Charles-Edwards L, Reinsberg SA, Leach MO. A complete distortion correction for MR images: I. Gradient warp correction. Phys Med Biol 2005;50:1343–61. https://doi.org/10.1088/0031-9155/50/7/001.

[28] Schenck JF. The role of magnetic susceptibility in magnetic resonance imaging: MRI magnetic compatibility of the first and second kinds. Med Phys 1996;23:815–50.

[29] Liney GP, Moerland MA. Magnetic resonance imaging acquisition techniques for radiotherapy planning. Semin Radiat Oncol 2014;24:160–8. https://doi.org/10.1016/j.semradonc.2014.02.014.

[30] Teeuwisse WM, Brink WM, Haines KN, Webb AG. Simulations of high permittivity materials for 7 T neuroimaging and evaluation of a new barium titanate-based dielectric. Magn Reson Med 2012;67:912–8. https://doi.org/10.1002/mrm.24176.

[31] Walker A, Liney G, Metcalfe P, Holloway L. MRI distortion: considerations for MRI based radiotherapy treatment planning. Australas Phys Eng Sci Med 2014;37:103–13. https://doi.org/10.1007/s13246-014-0252-2.

[32] Kraff O, Fischer A, Nagel AM, Monninghoff C, Ladd ME. MRI at 7 Tesla and above: demonstrated and potential capabilities. J Magn Reson Imaging 2015;41:13–33. https://doi.org/10.1002/jmri.24573.

[33] Marques JP, Gruetter R. New developments and applications of the MP2RAGE sequence - focusing the contrast and high spatial resolution R-1 mapping. PLoS One 2013;8:11. https://doi.org/10.1371/journal.pone.0069294.

[34] Hong C, Lee DH, Han BS. Characteristics of geometric distortion correction with increasing field-of-view in open-configuration MRI. Magn Reson Imaging 2014;32:786–90. https://doi.org/10.1016/j.mri.2014.02.007.

[35] Hashemi RH, Bradley Jr WG, Lisanti CJ. MRI: the Basics. 3rd ed. Philadelphia: Lippincott Williams and Wilkins; 2010.

[36] Wang D, Strugnell W, Cowin G, Doddrell DM, Slaughter R. Geometric distortion in clinical MRI systems Part II: correction using a 3D phantom. Magn Reson Imaging 2004;22:1223–32. https://doi.org/10.1016/j.mri.2004.08.014.

[37] Schmidt MA, Payne GS. Radiotherapy planning using MRI. Phys Med Biol. 2015;60:R323–61. https://doi.org/10.1088/0031-9155/60/22/r323.

[38] Jezzard P. The physical basis of spatial distortion in magnetic resonance images. In: Bankman IN, editor. Handbook of medical image processing and analysis. 2nd ed.Amsterdam: Elsevier/Academic Press; 2009. p. 499–514.

[39] Stanescu T, Jans HS, Wachowicz K, Fallone BG. Investigation of a 3D system distortion correction method for MR images. J Appl Clin Med Phys 2010;11:200–16.

[40] Stanescu T, Wachowicz K, Jaffray DA. Characterization of tissue magnetic susceptibility-induced distortions for MRIgRT. Med Phys 2012;39:7185–93. https://doi.org/10.1118/1.4764481.

[41] Rai R, Manton D, Jameson MG, Josan S, Barton MB, Holloway LC, et al. 3D printed phantoms mimicking cortical bone for the assessment of ultrashort echo time magnetic resonance imaging. Med Phys 2018;45:758–66. https://doi.org/10.1002/mp.12727.

[42] van Herk M. Errors and margins in radiotherapy. Semin Radiat Oncol 2004;14:52–64. https://doi.org/10.1053/j.semradonc.2003.10.003.

[43] Seravalli E, van Haaren PM, van der Toorn PP, Hurkmans CW. A comprehensive evaluation of treatment accuracy, including end-to-end tests and clinical data, applied to intracranial stereotactic radiotherapy. Radiother Oncol 2015;116:131–8. https://doi.org/10.1016/j.radonc.2015.06.004.